Geosciences and Geological and Petroleum Engineering Faculty Research & Creative Works

Geosciences and Geological and Petroleum Engineering

01 Mar 2020

Receiver Function Imaging of the 410 and 660 Km Discontinuities Beneath the Australian Continent

Kailun Ba

Stephen S. Gao
Missouri University of Science and Technology, sgao@mst.edu

Kelly H. Liu
Missouri University of Science and Technology, liukh@mst.edu

Fansheng Kong

et. al. For a complete list of authors, see *https://scholarsmine.mst.edu/geosci_geo_peteng_facwork/1826*

Recommended Citation

Receiver function imaging of the 410 and 660 km discontinuities beneath the Australian continent

Kailun Ba,[1] Stephen S. Gao [ORCID],[1] Kelly H. Liu,[1] Fansheng Kong[1,2] and Jianguo Song[3]

[1]*Geology and Geophysics Program, Missouri University of Science and Technology, Rolla, MO 65409, USA. E-mail: sgao@mst.edu*
[2]*Key Laboratory of Submarine Geosciences, State Oceanic Administration & Second Institute of Oceanography, Ministry of Natural Resources, Hangzhou* 310012, *China*
[3]*School of Geosciences, China University of Petroleum (East China), Qingdao* 266580, *China*

SUMMARY

To provide constraints on a number of significant controversial issues related to the structure and dynamics of the Australian continent, we utilize *P*-to-*S* receiver functions (RFs) recorded by 182 stations to map the 410 and 660 km discontinuities (d410 and d660, respectively) bordering the mantle transition zone (MTZ). The RFs are stacked in successive circular bins with a radius of 1° under a non-plane wave front assumption. The d410 and d660 depths obtained using the 1-D IASP91 earth model show a systematic apparent uplifting of about 15 km for both discontinuities in central and western Australia relative to eastern Australia, as the result of higher seismic wave speeds in the upper mantle beneath the former area. After correcting the apparent depths using the Australian Seismological Reference Model, the d410 depths beneath the West Australia Craton are depressed by ∼10 km on average relative to the normal depth of 410 km, indicating a positive thermal anomaly of 100 K at the top of the MTZ which could represent a transition from a thinner than normal MTZ beneath the Indian ocean and the normal MTZ beneath central Australia. The abnormally thick MTZ beneath eastern Australia can be adequately explained by subducted cold slabs in the MTZ. A localized normal thickness of the MTZ beneath the Newer Volcanics Province provides supporting evidence of non-mantle-plume mechanism for intraplate volcanic activities in the Australian continent.

Key words: Australia; Body waves; Cratons; Hotspots; Subduction zone processes.

1 INTRODUCTION

The Australian continent (Fig. 1) is a component of the Indo–Australian Plate, which was formed after the Permian breakup of Gondwana. At the present time, the continent is moving northward at a rate of 83 mm yr^{-1} in a fixed-hotspot frame (Gripp & Gordon 2002). The central and western portions of the Australian continent include three Archean–Proterozoic tectonic blocks (Pirajno & Bagas 2008): the North Australian Craton, West Australian Craton and South Australian Craton (Fig. 1). The eastern part of the continent consists of a number of younger units formed in the Phanerozoic that are collectively called Tasmanides (Betts *et al.* 2002; Direen & Crawford 2003).

Recent seismic tomography studies of the crust and upper mantle beneath the Australian continent and the topography of the lithosphere–asthenosphere boundary (LAB) indicate significant differences in wave speeds and lithospheric thickness between the cratonic regions and younger orogenic belts (Fig. 1, Yoshizawa & Kennett 2004; Fishwick *et al.* 2005; Conrad & Lithgow-Bertelloni 2006; Fishwick & Reading 2008; Fichtner *et al.* 2009; Rawlinson & Fishwick 2012; Kennett *et al.* 2013; Yoshizawa & Kennett 2015).

The depth of the LAB is greater than 200 km beneath the cratonic blocks, and reduces to about 100 km beneath the eastern margin of the continent (Conrad & Lithgow-Bertelloni 2006). Beneath the northeastern and eastern portions of the continent, seismic tomography images indicate the existence of high wave speed anomalies in the lower portion of the upper mantle and the mantle transition zone (MTZ), which are attributed to former subduction systems (Hall & Spakman 2002; Simmons *et al.* 2012). In particular, the large anomaly beneath northeastern Australia in the lower part of the upper mantle is interpreted to be the remnant of Pacific Plate subducted beneath the Melanesian arc between 45 and 25 Ma (Hall & Spakman 2002). However, due to the limited vertical resolution of the tomographic techniques and possible vertical smearing, whether the high wave speed anomalies extend to the MTZ remains controversial (Hall & Spakman 2002; Fichtner *et al.* 2009).

Another debated issue related to the structure and evolution of the Australian continent is the origin of intraplate volcanic activities in eastern Australia. The age of the volcanic rocks ranges from 4.5 Ma to younger than 5 kyr (Davies & Rawlinson 2014), and their origin is debated. Some studies attribute the volcanism to edge-driven convention associated with lithospheric thickness variations
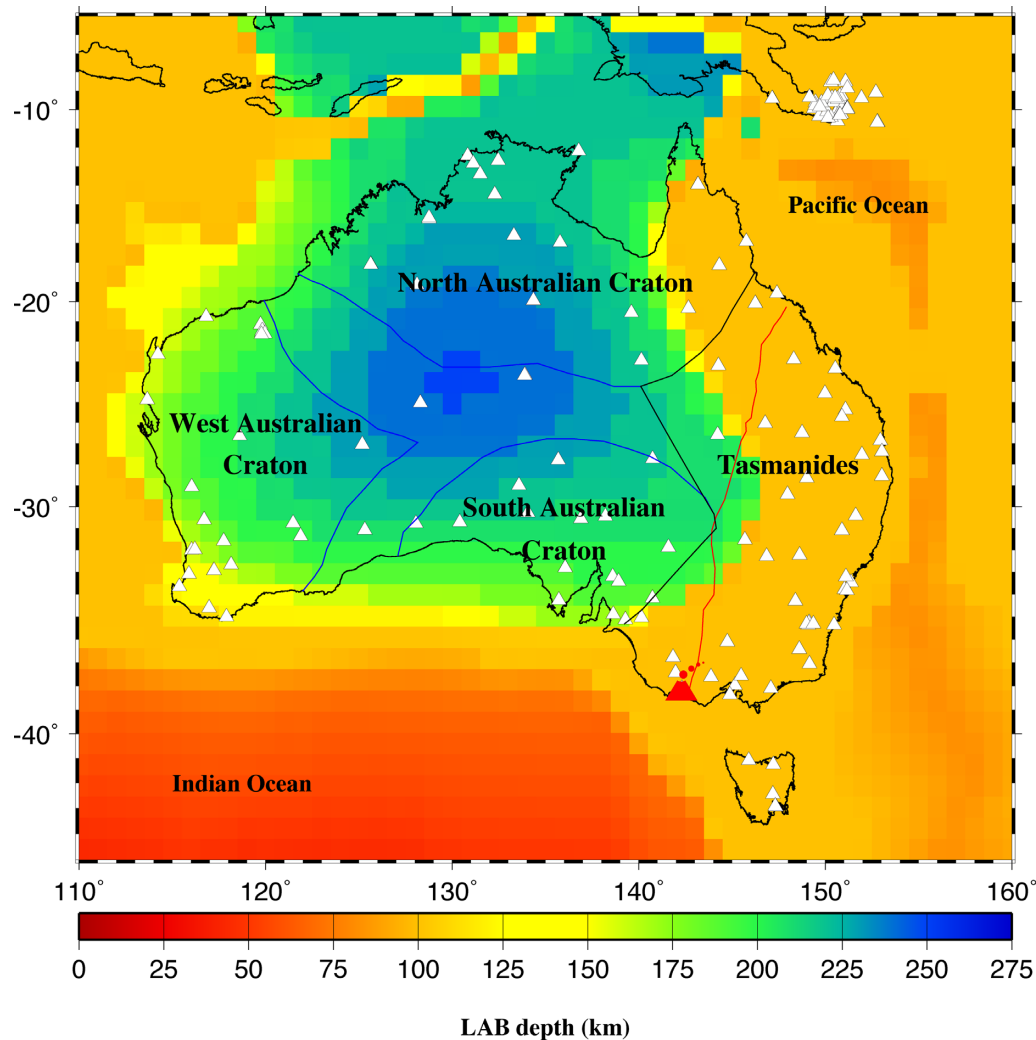
Figure 1. Broadband seismic stations (white triangles) used in this study, and major tectonic boundaries (blue and black lines) of Australia (Betts *et al.* 2002). The red line represents the hotspot track (Davies *et al.* 2015), and the red volcanic symbol denotes the Newer Volcanics Province. The background image shows the depth of the lithosphere–asthenosphere boundary (Conrad & Lithgow-Bertellon 2006).

(Demidjuk *et al.* 2007; Davies & Rawlinson 2014), while others propose that the magmas were generated by decompression melting (Demidjuk *et al.* 2007; Holt *et al.* 2013; Davies & Rawlinson 2014; Rawlinson *et al.* 2017). Another hypothesis associates the volcanism to a possible mantle plume that is responsible for producing the longest continental volcanic chain (the Cosgrove track) on Earth (Fig. 1; Montelli *et al.* 2006; Davies *et al.* 2015).

Most of the controversies are associated with the limited vertical resolving power of the seismic tomographic techniques (Foulger *et al.* 2013). As demonstrated by numerous previous studies (Anderson 1967; Flanagan & Shearer 1998; Litasov *et al.* 2005), the depth undulations of the 410 (d410) and 660 (d660) km discontinuities bordering the MTZ are functions of lateral variations of temperature and water content anomalies in the vicinity of the MTZ. Consequently, measured depths of the d410 and d660 have been utilized to provide independent constraints on various important controversial issues related to the structure and dynamics of the upper mantle and the MTZ, such as the depth extent of temperature perturbation of cold cratonic keels (Knapmeyer-Endrun *et al.* 2013; Sun *et al.* 2018; Makushkina *et al.* 2019), existence and geometry of subducted oceanic slabs in the MTZ (Dahm *et al.* 2017;

Yu *et al.* 2017; Taylor *et al.* 2018; Lai *et al.* 2019; van Stiphout *et al.* 2019), and the presence of thermal upwelling through the MTZ (Reed *et al.* 2016; Dahm *et al.* 2017; Kaviani *et al.* 2018). The d410 and d660 represent olivine to wadsleyite and ringwood-ite to bridgmanite and ferropericlase phase transitions, respectively (Ringwood 1975; Tschauner *et al.* 2014). The phase transition at the d410 has a positive Clapeyron slope and that at the d660 has a negative slope. If the temperature at the d660 increases to more than 1800 °C, the phase transition at the d660 becomes the transition from majorite to perovskite which is characterized by a positive Clapeyron of +1.0 MPa K^{-1} (Hirose 2002). Additionally, water in the MTZ reduces the sharpness of the discontinuities and leads to uplifted d410 and depressed d660 (Litasov *et al.* 2005). Increasing water content also results in reduction in seismic velocities (Wang *et al.* 2018).

The MTZ discontinuities beneath the Australian continent have been investigated by several studies (Flanagan & Shearer 1998; Lebedev *et al.* 2003; Lawrence & Shearer 2006). Using *P*-to-*S* receiver functions (RFs), Lebedev *et al.* (2003) measure MTZ thicknesses at seven stations and report large departures of up to ±30 km from the globally averaged value of 250 km. As part of a global-scale
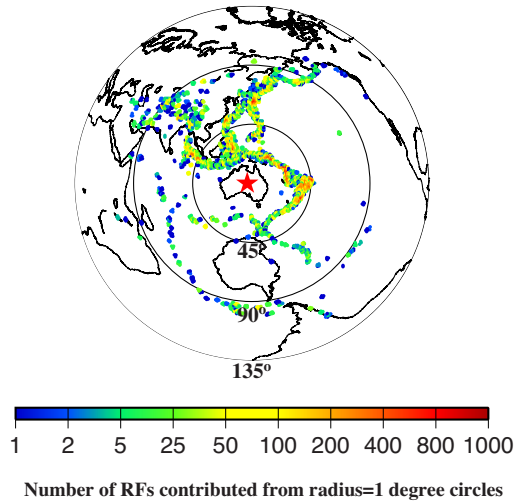
Figure 2. An azimuthal equidistant projection map showing distribution of events used in the study. The colour of the filled circles that have a 1° radius represents the number of RFs from earthquakes in the circle.

study, Flanagan & Shearer (1998) indicate that the MTZ beneath eastern Australia is thicker than that beneath the western part. The global-scale study of Lawrence & Shearer (2006) includes five stations in Australia, and finds a normal MTZ thickness beneath most part of the Australian continent.

In this study, we utilize a data set of more than 37 500 high-quality RFs, which represents an approximately 20-fold increase over the most recent MTZ studies in the area (Lebedev *et al.* 2003; Lawrence & Shearer 2006), to constrain the depths of the d410 and d660 beneath the Australian continent. The study is aimed at understanding the wave speed and thermal structure of the lower upper mantle and MTZ and providing constraints on the existence of subducted slabs and mantle upwelling that might be responsible for the widespread volcanism in eastern Australia.

2 DATA AND METHODS

The broad-band seismic data used in the study were requested from the Incorporated Research Institutions for Seismology (IRIS) Data Management Center (DMC) and were recorded by stations located in the area of 10°S to 45°S and 110°E to 155°E (Fig. 1), over the period of 1985–2017. The epicentral distances of the teleseismic events range from 30° to 100° (Fig. 2). To balance the quality and quantity of the requested data, we used cut-off magnitudes (M_c) determined by $M_c = 5.2 + (A–30)/(180–30)–D/700$, where A is the epicentral distance in degree and D is the depth of the earthquake in kilometre (Liu & Gao 2010).

The procedure used in this study for data processing, selection and stacking can be found in Gao & Liu (2014a) and is briefly outlined below. The seismograms were windowed 20 s before and 260 s after the first arrival time, calculated based on the IASP91 earth model (Kennett & Engdahl 1991), and were filtered in the frequency band of 0.02–0.2 Hz using a 4-pole, 2-pass Bessel filter. Seismograms with a first arrival signal-to-noise ratio of 4.0 or larger on the vertical component were selected and converted into radial RFs using the frequency-domain deconvolution procedure (Clayton & Wiggins 1976; Ammon 1991). The signal-to-noise ratio was defined as $|A_s|/|A_n|$, where $|A_s|$ is the maximum absolute amplitude on the vertical component in the time window of 2 s before and 2 s after the predicted *P*-wave first arrival using the IASP91 earth

model, and $|A_n|$ is the mean absolute amplitude of noise in the time window of 10–20 s before the predicted *P*-wave first arrival (Gao & Liu 2014b). We used an exponential weighting function with a half-width of 30 s centred at the PP theoretical arrival time to minimize the influence of the strong PP arrivals on the resulting RFs. A total of 37 524 RFs recorded by 182 stations from 5060 events were used in the study (Fig. 2).

The coordinates of the ray piercing point for each of the RFs were calculated at 535 km depth, which is the mean depth of the two MTZ discontinuities. RFs within the same 1-degree radius circular bins were then moveout corrected and stacked. The size of the circular bins is comparable to that of the first Fresnel zone for *P*-to-*S* converted waves at 535 km depth. For instance, assuming a dominant frequency of 0.1 Hz and using the shear wave velocities in the IASP91 earth model, the radius of the first Fresnel zone of the *P*-to-*S* converted wave is 111.8 km which is almost exactly 1°. The moveout correction takes into consideration of the ray parameters dependence of the differential arrival times between the direct *P* wave and *P*-to-*S* converted wave (Dueker & Sheehan 1998). Unlike most previous MTZ discontinuity studies, which assume a plane wave front, this study assumes a non-plane wave front which takes consideration of the slight difference in the ray parameters for the direct *P* and *P*-to-*S* converted phases, and consequently improves the accuracy of the predicted arrival times of the converted phase (Gao & Liu 2014a), leading to more accurately determined discontinuity depths and greater stacking amplitudes relative to approaches assuming a plane wave front. We used the bootstrap resampling procedure with 50 iterations to estimate the mean and standard deviation (SD) of the discontinuity depths at each of the bins (Efron & Tibshirani 1986; Liu *et al.* 2003).

After automatic picking of the depths of the two discontinuities in the depth ranges of 390–450 km and 630–690 km for the d410 and d660, respectively, we manually checked the results and if necessary, adjusted the picking ranges and rejected bins with weak arrivals or ambiguous peaks. We initially used the 1-D IASP91 standard earth model (Kennett & Engdahl 1991) to perform moveout corrections and time-depth conversion, and thus the resulting discontinuity depths are apparent rather than true depths. The resultant apparent depths of the discontinuities were subsequently corrected using the Australian Seismological Reference Model (AuSREM, Kennett *et al.* 2013), which includes both *P* and *S* wave speeds in the depth range of 50–300 km, and the effects of crustal thickness variations in the 0–50 km depth range, to reduce the influence of upper mantle and crustal wave speed anomalies on the observed depths using the procedure proposed by Gao & Liu (2014a).

3 RESULTS

A total of 522 bins (Fig. 3) with observable d410 or d660 peaks are obtained, among which 469 bins possess reliable peaks for both the d410 and d660. Fig. 4 shows examples of the resulting depth series along three latitudinal lines. Similar plots for all the 33 latitudinal lines (from 10°S to 42°S with an increment of 1°) can be found in Figs S1–S33. We used the continuous curvature surface gridding algorithm (Smith & Wessel 1990) to generate continuous images for the discontinuity depths and MTZ thickness (Fig. 5). The resulting apparent depths show a clear difference between the cratonic areas in central and western Australia and the younger units in eastern Australia, approximately separated by the 140°E longitudinal line (Fig. 5).
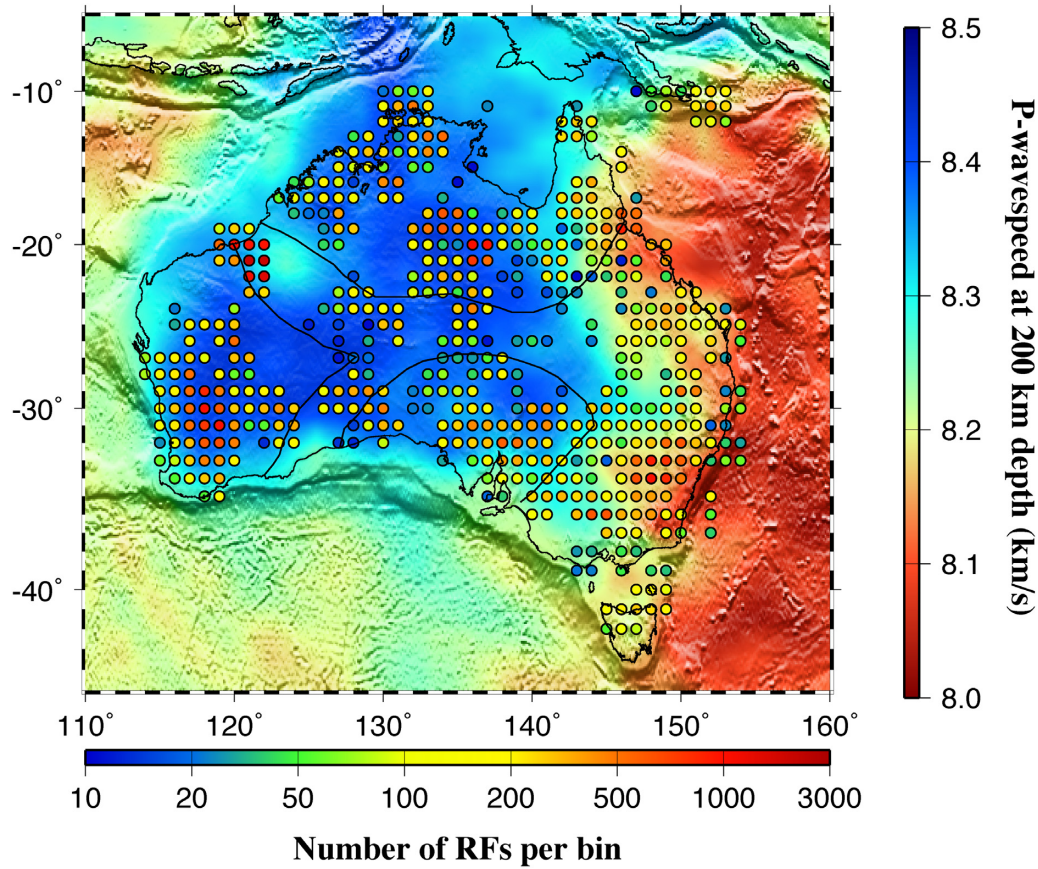
Figure 3. Distribution of the centre of radius = 1° circular bins (circles). The colour of the circles represents the number of RFs inside the circular bins. The background image shows *P*-wave speeds at 200 km depth in the AuSREM (Kennett *et al.* 2013).
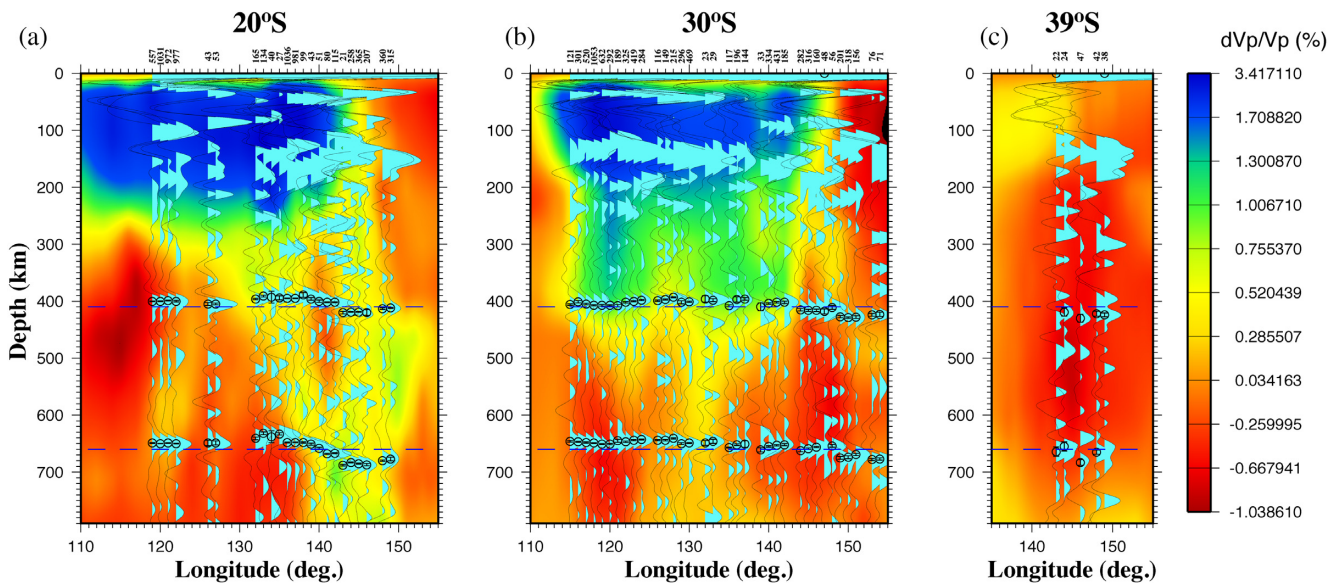

Figure 4. Results of stacking the RFs along three latitudinal profiles (20°S, 30°S and 39°S). The black dots and error bars indicate the mean depths and standard deviations. The number atop each trace indicates the number of RFs in the bin. Note that the profile in (c) traverses the Newer Volcanics Province. The background image shows *P*-wave velocity anomalies relative to IASP91 (Lu *et al.* 2019).
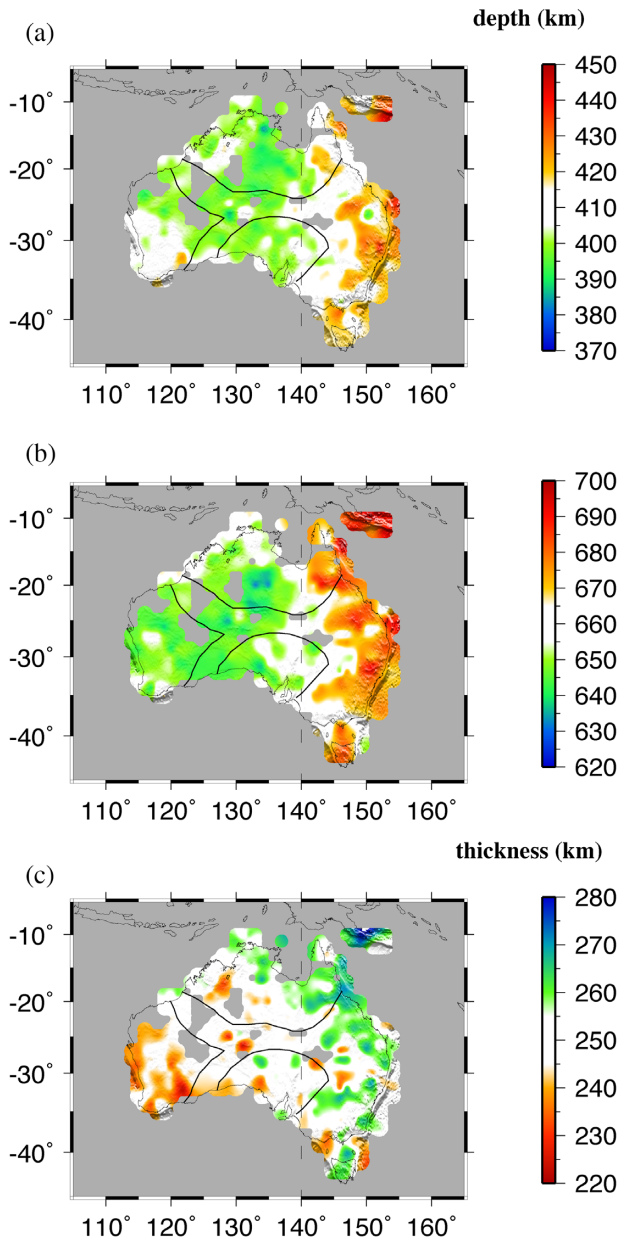
(a)

(b)

(c)

Figure 5. (a) Resulting d410 apparent depths. (b) d660 apparent depths. (c) MTZ thickness. The dashed line approximately separates the areas with shallower than normal discontinuities to the west and deeper than normal discontinuities to the east.

3.1 Apparent depths of the MTZ discontinuities

The average apparent depth of the d410 and d660 for the entire area is 407.5 ± 9.9 and 659.1 ± 13.5 km, respectively, and the mean MTZ thickness is 251.6 ± 8.5 km which is almost identical to the global average of 250 km in the IASP91 earth model. In central and western Australia, the observed d410 apparent depths range from 385 to 424 km, with a mean value of 401.3 ± 5.8 km. The corresponding values for the d660 are 632 to 666 km and 650.1 ± 6.5 km, and the mean MTZ thickness is 248.1 ± 6.9 km. In eastern Australia, the d410 and the d660 apparent depths range from 395 to 442 km and 642 to 698 km, respectively, and the mean depths are 415.6 ± 8.4 km and 671.8 ± 10.1 km, respectively, with a mean MTZ thickness of 255.3 ± 8.8 km (Fig. 5).
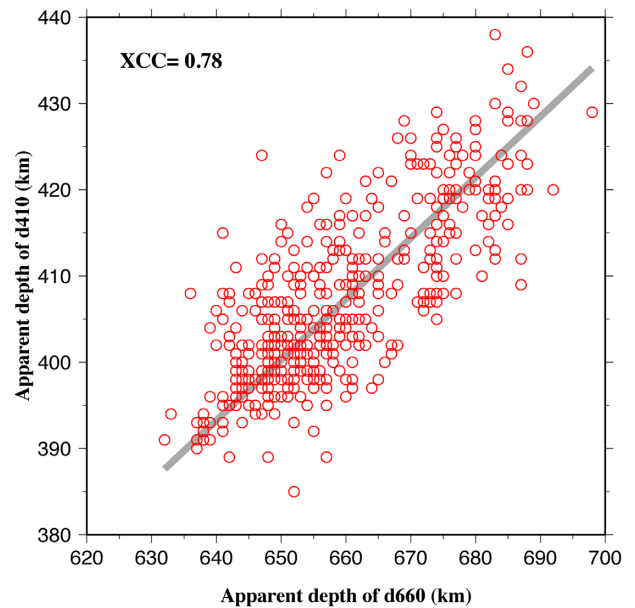

Figure 6. The d410 apparent depths plotted against the d660 apparent depths. The grey line represents the line of best fit. XCC, cross correlation coefficient.

The cross-correlation coefficient (XCC) between the apparent depths of the d410 and d660 can be used to estimate the influence of wave speed anomalies in the upper mantle on the observed depths, because they affect the apparent depths of both discontinuities equally (e.g. Flanagan & Shearer 1998; Gao & Liu 2014b). If the depth variations are entirely caused by temperature or water content anomalies in the MTZ, given the opposite sign of the Clapeyron slopes of the d410 and d660 and the opposite effects of water on the depth variation of the d410 and d660 (Litasov *et al.* 2005), a negative XCC is expected. The XCC of the apparent depths for the study area is 0.78 (Fig. 6), indicating that upper mantle wave speed anomalies have a significant influence on the apparent depths of the discontinuities. This is consistent with the negative correlation (with a XCC of -0.72) between the apparent d410 depths and the Vp anomalies in the AuSREM model.

3.2 Wave speed-corrected depths

In order to make complete wave speed corrections to the apparent depths of the d410 and d660, 3-D high resolution *P*- and *S*-wave velocity models extending from the surface to the bottom of the MTZ are required. To our knowledge, such models are not available for the study area. Arguably the most suitable existing velocity model for this purpose is AuSREM (Kennett *et al.* 2013), which has a *P* and an *S* wave speed component and covers the entire study area. Unfortunately, the maximum depth in the model is 300 km, with an interval depth of 25 km. Although the depth coverage of AuSREM is not ideal, we have used it to perform wave speed corrections to explore the possibility that wave speed anomalies in the top 300 km are largely responsible for the observed lateral variations of the apparent depths. The procedure that we used for the correction is the same as that used in Gao & Liu (2014b) for making wave speed corrections for the contiguous United States. To perform the correction, the mean velocity anomalies above 300 km (which is the maximum depth of the AuSREM model) is first computed for each of the bins. Then equation 2 in Gao & Liu (2014b) is used to convert
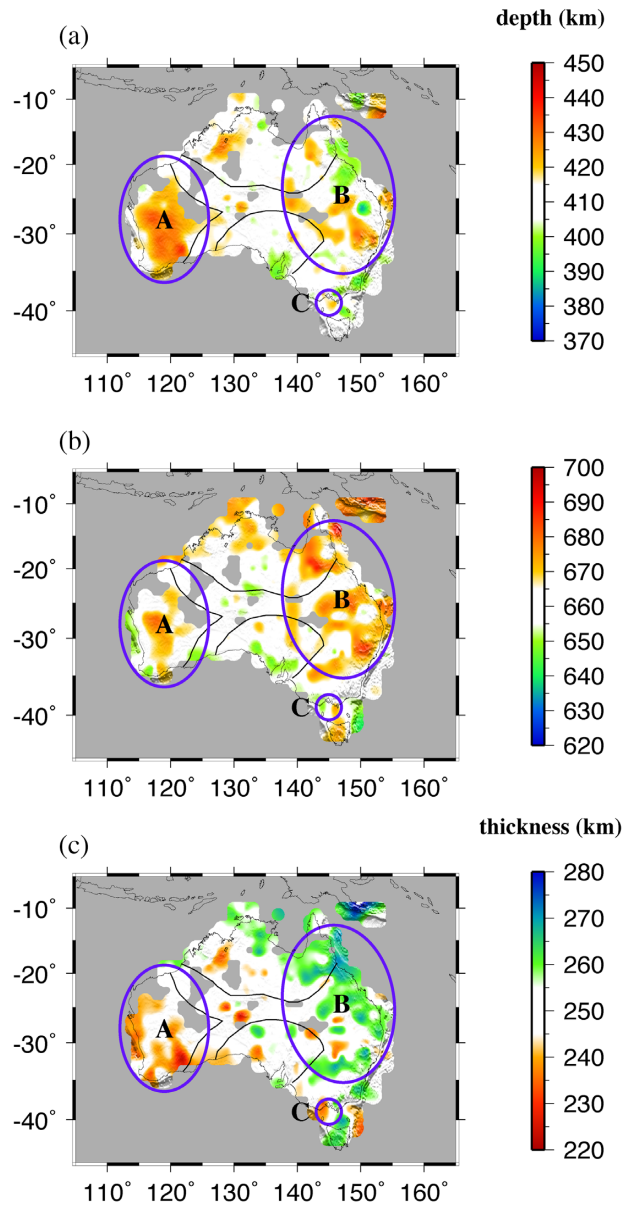
Figure 7. Same as Fig. 5 but for the corrected depths based on the AuSREM model.

Figure 8. Same as Fig. 6 but for the wave speed corrected depths using the AuSREM model.

the apparent depths of the d410 and d660 into true depths. After the correction, the mean depth of the d410 is 413.1 ± 7.6 km, that of the d660 is 664.7 ± 7.6 km, and the mean MTZ thickness remains as 251.6 ± 8.5 km because the velocity model does not extend to the MTZ (Fig. 7). The XCC reduces from 0.78 to 0.38 (Fig. 8), suggesting that wave speed anomalies in the top 300 km play a significant role in the variations of the observed apparent depths of the MTZ discontinuities. Additionally, the ∼15 km apparent difference between eastern Australia and the rest of the continent (Fig. 5) has greatly reduced (Fig. 7) after the correction, suggesting that AuSREM realistically reflects the true wave speed structure of the study area. Only minor velocity anoamlies are suggested in the 300–410 km dpeth range beneath the study area in most global-scale tomography models (e.g. Lu *et al.* 2019).

Because the AuSREM model has a maximum depth of 300 km, we next correct the apparent depths and MTZ thickness using a newly available global model, TX2019VpVs (Lu *et al.* 2019), which
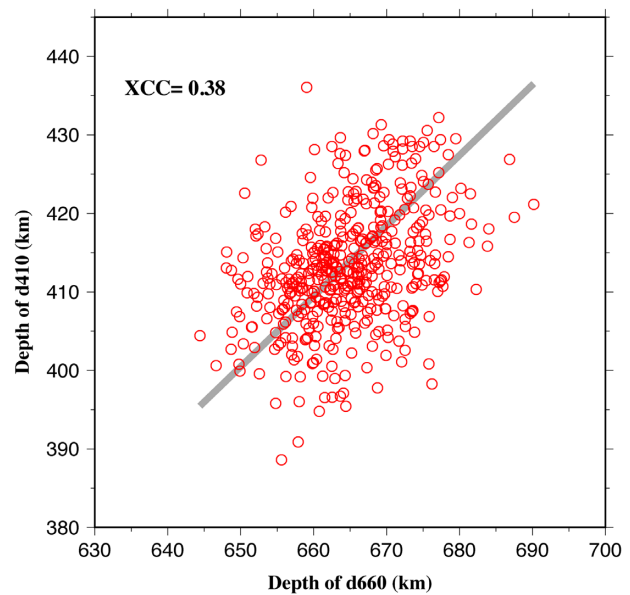
contains both *P*- and *S*-wave velocity anomalies relative to IASP91 for the surface to the core mantle boundary, to explore if there are significant velocity variations between 300 km and the d660. The resulting MTZ thickness (Fig. 9c) distribution is almost identical to that obtained using the AuSREM model (Fig. 7c). The corrected d410 and d660 depths using TX2019VpVs, on the other hand, are slightly deeper than normal for almost all of the study area, suggesting a possible overcorrection. Given this fact and the similarities in the resulting corrected MTZ thickness distributions from the two models, in the following the corrected depths using AuSREM are discussed.

The MTZ thickness and corrected d410 and d660 depths beneath central Australia are mostly comparable to the global averages (within ±5 km; Fig. 7). Beneath West Australian Craton (Region A in Fig. 7), where the mean values of the corrected d410 and d660 depths and the MTZ thickness are 420.2 ± 6.9, 664.4 ± 6.7 and 244.1 ± 5.7 km, respectively (Table 1). The thinning of the MTZ is mostly caused by a greater depression of the d410 than the d660 (Figs 7a and b). The second region (Region B) includes eastern Australia except for the Newer Volcanics Province in SE Australia. In this area, the d660 shows a greater depression than the d410, with mean values of 412.5 ± 7.5 and 668.4 ± 7.6 km, respectively, leading to a MTZ that is about 6 km thicker than the globally averaged value of 250 km. The third area that is dominated by anomalous d410 and d660 depths is the Newer Volcanics Province (Region C) which is characterized by a d410 that is 7 km deeper and a d660 that is similar to the normal values, resulting in an MTZ that is about 2 km thinner than normal. Note that for the two bins in Region C, the d660 depths have a 18 km (656 and 674) difference (Fig. 4c). The bin with the thinnest MTZ has a thickness of 243 km.

4 DISCUSSION

In this section, we utilize the corrected MTZ discontinuities depths to discuss the influence of the thick lithosphere on MTZ temperature beneath the West Australian Craton, possible existence of subducted oceanic slabs in the MTZ beneath eastern Australia, and provide constraints on the proposed mantle plume beneath the
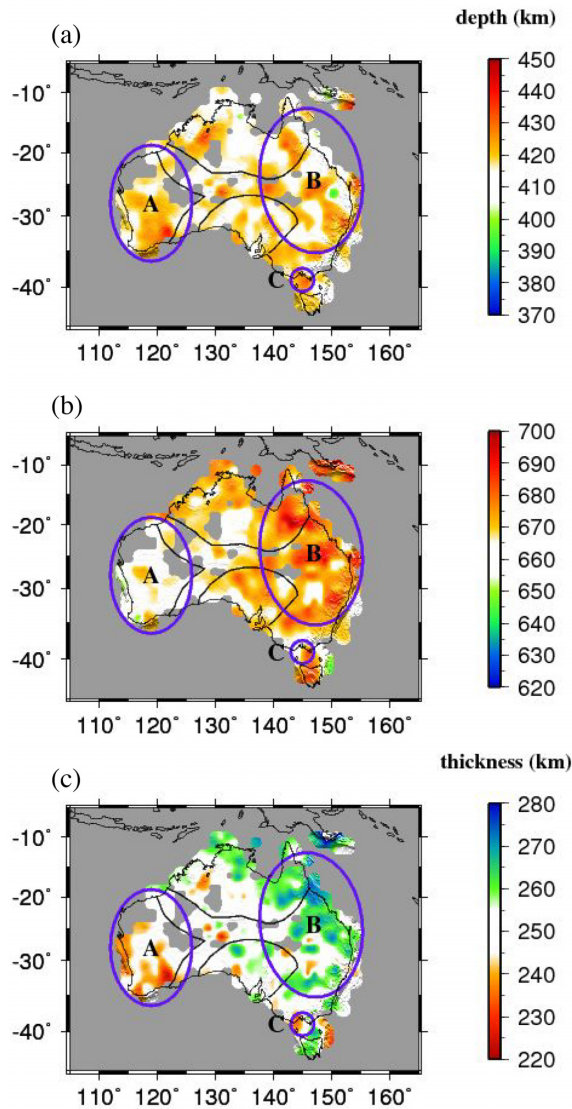
Figure 9. Same as Fig. 5 but for the corrected depths based on the TX2019VpVs model.

Newer Volcanics Province. Besides temperature anomalies, both water content and Fe/Mg ratio can also affect the depth of the discontinuities (Litasov *et al.* 2005; Frost 2008). For instance, a higher Fe content leads to a shallower d410. However, both higher water and Fe contents cause a broader phase transition across the discontinuities, leading to a reduction in the amplitude of the *P*-to-S converted phase. As shown in Figs 4 and S1–S33, no systematic spatial variations can be observed in the stacking amplitudes, suggesting that both water and Fe content anomalies do not play a significant role in the observed depth variations of the discontinuities.

4.1 Possible influence of the thick lithosphere beneath the West Australian Craton on MTZ temperature

The wave speed corrected depths (Fig. 7) show that both discontinuities are depressed beneath the West Australian Craton, and the d410 depresses about 6 km more than the d660, resulting in a thinner than normal MTZ by 6 km on average and a maximum value of 25 km. Under the assumption that the wave speed correction for the upper 300 km using AuSREM is accurate, the depression of the d410 can

be explained by a low wave speed layer extending from 300 km to the middle of the MTZ and the corresponding higher-than-normal temperatures. If we assume a γ factor, which is the relative *S* and *P* wave speed anomaly ratio, of 2.0 (Gao & Liu 2014b) and a Clapeyron slope of +2.9 MPa K^{-1} for the d410 (Bina & Helffrich 1994) and −1.3 MPa K^{-1} for the d660 (Fei *et al.* 2004), a *Vp* anomaly of −0.56 per cent in the depth range of 300–535 km would lead to an apparent depression of 2 and 4 km for the d410 and d660, respectively. Using the relationship of d*Vp*/d*T* = −0.00048 km (s K)$^{-1}$ (Deal *et al.* 1999), the low-wave speed anomaly corresponds to an approximately +100 K thermal anomaly. This positive thermal anomaly results in an 8 km depression of the d410. Thus, the net depression of the d410 is about 10 km and that of the d660 is about 4 km, which are consistent with the observed results. One of the possible causes of the observation is that the thermal insulation effects of the thick lithosphere extending to the middle MTZ (Grigne & Labrosse 2001). However, while such effect has been proposed to explain tomographically imaged sublithospheric low wave speeds beneath some cratonic areas such as North America (Porritt *et al.* 2015), its existence requires an insignificant displacement between the lithosphere and the underlain deeper mantle for an extended long period, which may not be possible given the relatively fast movement of the Australian continent since the breakup of the Gondwana. In addition, such a low velocity layer is not identified beneath most cratonic areas such as the Kaapvaal and Zimbabwe cratons using seismic tomography (Fouch *et al.* 2004) and RF stacking (Sun *et al.* 2018).

Another mechanism responsible for the observed MTZ thinning is an extension of the hotter MTZ beneath oceanic areas. Most previous studies involving both continental and oceanic areas (e.g. Flanagan & Shearer 1998; Gu & Dziewonski 2002) find that the MTZ beneath the oceanic areas is about 6–8 km thinner than the adjacent continental areas. The MTZ beneath the marginal areas of the continents is thinner than the continental interior and may represent a transition from the thinner ocean MTZ to the normal continental MTZ. For instance, beneath the western edge of the North American continent, a RF study using the same technique as what is used in this study finds an MTZ thickness that is about 10 km thinner than the central part of the continent (Gao & Liu 2014b). Similar to the West Australian Craton, the thinning of the MTZ beneath the western margin of North America is mostly caused by a more depressed d410 than the d660, suggesting a hotter upper MTZ.

4.2 Cold slabs in the lower MTZ beneath eastern Australia

Eastern Australia is dominated by an MTZ that is up to 28 km thicker than normal, with a mean value of about 6 km thicker. This MTZ thickening is mostly related to a greater depression of the d660 than the d410 (Table 1). The simplest model accounting for the 6 km thickening is a −50 °C temperature anomaly in the MTZ (estimated using a Clapeyron slope of 2.9 and −1.3 MPa K^{-1} for the d410 and d660, respectively), probably from oceanic slabs of the Pacific Plate subducted over the past 25 Myr (Crook & Belbin 1978; Hall & Spakman 2002; Simmons *et al.* 2012). The thicker MTZ beneath this area provides independent evidence for the subduction and stagnation of oceanic slabs in the MTZ, and is consistent with conclusions from most of the previous seismic tomography studies (Hall & Spakman 2002; Simmons *et al.* 2012; Obayashi *et al.* 2013). Alternatively, the slight thickening of the MTZ could indicate a higher level of water content (Litasov *et al.* 2005). However, a

Table 1. Resulting apparent and wave speed-corrected d410 and d660 depths and MTZ thickness for the whole area and each of the three regions with anomalous MTZ thickness.

Region	Whole area	A	B	C
Apparent d410 depth (km)	407.5 ± 9.9	404.7 ± 5.2	414.9 ± 8.4	426.0 ± 5.7
Apparent d660 depth (km)	659.1 ± 13.5	648.9 ± 5.5	670.8 ± 10.4	674.0 ± 12.7
Apparent MTZ thickness (km)	251.6 ± 8.5	244.1 ± 5.7	255.9 ± 8.3	248.0 ± 7.1
Corrected d410 depth (km)	413.1 ± 7.6	420.2 ± 6.9	412.5 ± 7.5	416.9 ± 5.4
Corrected d660 depth (km)	664.7 ± 7.6	664.4 ± 6.7	668.4 ± 7.6	664.9 ± 12.5
Corrected MTZ thickness (km)	251.6 ± 8.5	244.1 ± 5.7	255.9 ± 8.3	248.0 ± 7.1

higher water content normally corresponds to lower wave speeds (Wang *et al.* 2018) which are not suggested by previous seismic tomographic images (e.g. Hall & Spakman 2002; Simmons *et al.* 2012).

4.3 Constraints on the formation mechanism of the New Volcanics Province

Imaging the MTZ discontinuities can provide independent constraints on the mechanism of the intraplate volcanic activities (Reed *et al.* 2016; Dahm *et al.* 2017; Kaviani *et al.* 2018). In the New Volcanics Province (Region C), the depth series at the centre of this area (the middle trace in Fig. 4c) has two possible d660 arrivals with comparable amplitude. If the upper arrival is used as the *P*-to-*S* conversion from the d660, the MTZ thickness is 230 km which is the result of a 16 km uplift of the d660 and 4 km depression of the d410 (after wave speed correction). Using a Clapeyron slope of -1.3 MPa K^{-1} for the d660 (Fei *et al.* 2004), the 16 km uplift would require a temperature anomaly of about $+450$ K. Because this anomaly would cause a d410 depression as large as 37 km (which is much greater than the observed 4 km) if it extends to the top of the MTZ, it must only exist in a thin layer surrounding the d660. Such a high temperature (more than 2000 K) would facilitate a phase transition from majorite to perovskite which has a positive Clapeyron of $+1.0$ MPa K^{-1} (Hirose 2002) and consequently lead to a depression rather than the observed uplift of the d660. Therefore, we conclude that the upper arrival is unlikely representing the d660.

The lower arrival has a wave speed-corrected depth of 667 km. Together with the 4 km depression of the d410, the resulting MTZ thickness is merely ~3 km thicker than normal, suggesting a close to normal MTZ temperature. The apparent depression of 14 km of the d410 corresponds to a mean upper mantle *Vp* anomaly of -1.0 per cent which is comparable to results from seismic tomography studies (e.g. Rawlinson & Kennett 2008; Rawlinson *et al.* 2017). These observations are consistent with the non-plume mechanism for the intraplate volcanic chain in eastern Australia (Demidjuk *et al.* 2007; Holt *et al.* 2013; Davies & Rawlinson 2014; Rawlinson *et al.* 2017).

5 CONCLUSIONS

In this study, we use 37 524 high-quality RFs from 182 seismic stations to map the topography of the 410 and 660 discontinuities beneath the Australian continent. When the 1-D IASP91 earth model is used for moveout correction and time-depth conversion, the resulting apparent depth of the d410 beneath eastern Australia is about 5 km deeper than normal, and that beneath the central and western Australia is 10 km shallower than normal, suggesting slower and faster mean upper mantle wave speeds beneath eastern and central/western Australia, respectively. After correcting the

apparent depths using AuSREM, the systematic difference between the two areas reduces, and anomalous thermal and wave speed conditions in the MTZ for three of areas can be extracted from the wave speed-corrected depths. The deeper than normal d410 and the thin MTZ beneath the West Australian Craton are similar to what has been reported beneath some other continental margins and may present a transition from a hotter than normal oceanic MTZ to the normal MTZ beneath central Australia. Beneath eastern Australia, the thicker than normal MTZ provides independent support for the existence of cold slabs in the MTZ. The normal MTZ thickness beneath the Newer Volcanics Province is consistent with the non-plume mechanism of the intraplate volcanic chain beneath eastern Australia.

REFERENCES

Ammon, C.J., 1991. The isolation of receiver effects from teleseismic P waveforms, *Bull. seism. Soc. Am.,* **81**(6), 2504–2510.

Anderson, D.L., 1967. Phase changes in the upper mantle, *Science,* **157**(3793), 1165–1173.

Betts, P.G., Giles, D., Lister, G.S. & Frick, L.R., 2002. Evolution of the Australian lithosphere, *Aust. J. Earth Sci.,* **49**(4), 661–695.

Bina, C.R. & Helffrich, G., 1994. Phase transition Clapeyron slopes and transition zone seismic discontinuity topography, *J. geophys. Res.,* **99**(B8), 15 853–15 860.

Clayton, R.W. & Wiggins, R.A., 1976. Source shape estimation and deconvolution of teleseismic bodywaves, *Geophys. J. Int.,* **47**(1), 151–177.

Conrad, C.P. & Lithgow-Bertelloni, C., 2006. Influence of continental roots and asthenosphere on plate-mantle coupling, *Geophys. Res. Lett.,* **33**, L05312, doi:10.1029/2005GL025621.

Crook, K.A. & Belbin, L., 1978. The southwest Pacific area during the last 90 million years, *J. Geol. Soc. Aust.,* **25**(1-2), 23–40.

Dahm, H.H., Gao, S.S., Kong, F. & Liu, K.H., 2017. Topography of the mantle transition zone discontinuities beneath Alaska and its geodynamic implications: constraints from receiver function stacking, *J. geophys. Res.,* **122**, 10 352–10 363.

Davies, D.R. & Rawlinson, N., 2014. On the origin of recent intraplate volcanism in Australia, *Geology,* **42**(12), 1031–1034.

Davies, D.R., Rawlinson, N., Iaffaldano, G. & Campbell, I.H., 2015. Lithospheric controls on magma composition along Earth's longest continental hotspot track, *Nature,* **525**(7570), 511–514.

Deal, M.M., Nolet, G. & van der Hilst, R.D., 1999. Slab temperature and thickness from seismic tomography: 1. Method and application to Tonga, *J. geophys. Res.,* **104**(B12), 28789–28802.

Demidjuk, Z., Turner, S., Sandiford, M., George, R., Foden, J. & Etheridge, M., 2007. U-series isotope and geodynamic constraints on mantle melting processes beneath the Newer Volcanic Province in South Australia, *Earth planet. Sci. Lett.,* **261**(3), 517–533.

Direen, N.G. & Crawford, A.J., 2003. The Tasman Line: Where is it, what is it, and is it Australia's Rodinian breakup boundary? *Austr. J. Earth Sci.,* **50**(4), 491–502.

Dueker, K.G. & Sheehan, A.F., 1998. Mantle discontinuity structure beneath the Colorado Rocky Mountains and high plains, *J. geophys. Res: Solid Earth ,* **103** (B4), 7153–7169, httpL//doi.org/10.1029/97JB03509.

Efron, B. & Tibshirani, R., 1986. Bootstrap methods for standard errors, confidence intervals, and other measures of statistical accuracy, *Stat. Sci.,* **1**(1), 54–75, doi:10.1214/ss/1177013815.

Fei, Y. *et al.*, 2004. Experimentally determined postspinel transformation boundary in Mg_2SiO_4 using MgO as an internal pressure standard and its geophysical implications, *J. geophys. Res.,* **109**, B02305, doi:10.1029/2003JB002562.

Fichtner, A., Kennett, B.L.N., Igel, H. & Bunge, H.P., 2009. Full seismic waveform tomography for upper-mantle structure in the Australasian region using adjoint methods, *Geophys. J. Int.,* **179**(3), 1703–1725.

Fishwick, S., Kennett, B.L.N. & Reading, A.M., 2005. Contrasts in lithospheric structure within the Australian craton—insights from surface wave tomography, *Earth planet. Sci. Lett.,* **231**(3-4), 163–176.

Fishwick, S. & Reading, A.M., 2008. Anomalous lithosphere beneath the Proterozoic of western and central Australia: a record of continental collision and intraplate deformation? *Precamb. Res.,* **166**(1), 111–121.

Flanagan, M.P. & Shearer, P.M., 1998. Global mapping of topography on transition zone velocity discontinuities by stacking SS precursors, *J. geophys. Res.,* **103**, 2673–2692.

Fouch, M.J., James, D.E., VanDecar, J.C. & Van der Lee, S., Kaapvaal Seismic Group, 2004. Mantle seismic structure beneath the Kaapvaal and Zimbabwe Cratons, *S. Afr. J. Geol.,* **107**(1-2), 33–44.

Foulger, G.R. *et al.*, 2013. Caveats on tomographic images, *Terra Nova,* **25**(4), 259–281.

Frost, D.J., 2008. The upper mantle and transition zone, *Elements,* **4** (3), 171–176.

Gao, S.S. & Liu, K.H., 2014a. Imaging mantle discontinuities using multiply-reflected P-to-S conversions, *Earth planet. Sci. Lett.,* **402**, 99–106.

Gao, S.S. & Liu, K.H., 2014b. Mantle transition zone discontinuities beneath the contiguous United States, *J. geophys. Res.,* **119**, 6452–6468.

Grigne, C. & Labrosse, S., 2001. Effects of continents on Earth cooling: thermal blanketing and depletion in radioactive elements, *Geophys. Res. Lett.,* **28**(14), 2707–2710.

Gripp, A.E. & Gordon, R.G., 2002. Young tracks of hotspots and current plate velocities, *Geophys. J. Int.,* **150**(2), 321–361.

Gu, Y.J. & Dziewonski, A.M., 2002. Global variability of transition zone thickness, *J. geophys. Res.,* **107**(B7), ESE-2.

Hall, R. & Spakman, W., 2002. Subducted slabs beneath the eastern Indonesia–Tonga region: insights from tomography, *Earth planet. Sci. Lett.,* **201**(2), 321–336.

Hirose, K., 2002. Phase transitions in pyrolitic mantle around 670-km depth: implications for upwelling of plumes from the lower mantle, *J. geophys. Res.,* **107**(B4), 2078, doi:10.1029/2001JB000597.

Holt, S.J., Holford, S.P. & Foden, J., 2013. New insights into the magmatic plumbing system of the South Australian Quaternary Basalt province from 3D seismic and geochemical data, *Austr. J. Earth Sci.,* **60**(8), 797–817.

Kaviani, A., Sandvol, E., Moradi, A., Rümpker, G., Tang, Z. & Mai, P.M., 2018. Mantle transition zone thickness beneath the Middle East: evidence for segmented Tethyan slabs, delaminated lithosphere, and lower mantle upwelling, *J. geophys. Res.,* **123**, 4886–4905.

Kennett, B.L.N. & Engdahl, E.R., 1991. Traveltimes for global earthquake location and phase identification, *Geophys. J. Int.,* **105**, 429–465.

Kennett, B.L.N., Fichtner, A., Fishwick, S. & Yoshizawa, K., 2013. Australian Seismological Reference Model (AuSREM): mantle component, *Geophys. J. Int.,* **192**(2), 871–887.

Knapmeyer-Endrun, B., Krüger, F., Legendre, C.P. & Geissler, W.H., PASSEQ Working Group, 2013. Tracing the influence of the Trans-European Suture Zone into the mantle transition zone, *Earth planet. Sci. Lett.,* **363**, 73–87.

Lai, Y., Chen, L., Wang, T. & Zhan, Z., 2019. Mantle transition zone structure beneath Northeast Asia from 2-D triplicated waveform modeling: Implication for a segmented stagnant slab, *J. geophys. Res.,* **124**, 1871–1888.

Lawrence, J.F. & Shearer, P.M., 2006. A global study of transition zone thickness using receiver functions, *J. geophys. Res.,* **111**(B6), doi:10.1029/2005JB003937.

Lebedev, S., Chevrot, S. & Van der Hilst, R.D., 2003. Correlation between the shear-speed structure and thickness of the mantle transition zone, *Phys. Earth planet. Inter.,* **136**, 25–40.

Litasov, K.D., Ohtani, E., Sano, A., Suzuki, A. & Funakoshi, K., 2005. Wet subduction versus cold subduction, *Geophys. Res. Lett.,* **32**, L13312, doi:10.1029/2005GL022921.

Liu, K.H. & Gao, S.S., 2010. Spatial variations of crustal characteristics beneath the Hoggar swell, Algeria, revealed by systematic analyses of receiver functions from a single seismic station, *Geochem., Geophys., Geosys.,* **11**(8), doi:10.1029/2010GC003091.

Liu, K.H., Gao, S.S., Silver, P.G. & Zhang, Y., 2003. Mantle layering across central South America, *J. geophys. Res.,* **108**(B11), 2510, doi:10.1029/2002JB002208.

Lu, C., Grand, S.P., Lai, H. & Garnero, E.J., 2019. TX2019slab: a new P and S tomography model incorporating subducting slabs, *J. geophys. Res.,* **124**, doi:10.1029/2019JB017448.

Makushkina, A., Tauzin, B., Tkalčić, H. & Thybo, H., 2019. The mantle transition zone in Fennoscandia: enigmatic high topography without deep mantle thermal anomaly, *Geophys. Res. Lett.,* **46**, 3652–3662.

Montelli, R., Nolet, G., Dahlen, F.A. & Masters, G., 2006. A catalogue of deep mantle plumes: new results from finite-frequency tomography, *Geochem., Geophys., Geosys.,* **7**(11), doi:10.1029/2006GC001248.

Obayashi, M., Yoshimisu, J., Nolet, G., Fukao, Y., Shiobara, H., Sugioka, H., Miyamachi, H. & Gao, Y., 2013. Finite frequency whole mantle P wave tomography: Improvement of subducted slab images, *Geophys. Res. Lett.,* **40**(21), 5652–5657.

Pirajno, F. & Bagas, L., 2008. A review of Australia's Proterozoic mineral systems and genetic models, *Precamb. Res.,* **166**(1-4), 54–80.

Porritt, R.W., Miller, M.S. & Darbyshire, F.A., 2015. Lithospheric architecture beneath Hudson Bay, *Geochem., Geophys., Geosyst.,* **16**(7), 2262–2275.

Rawlinson, N., Davies, D.R. & Pilia, S., 2017. The mechanisms underpinning Cenozoic intraplate volcanism in eastern Australia: insights from seismic tomography and geodynamic modeling, *Geophys. Res. Lett.,* **44**(19), 9681–9690.

Rawlinson, N. & Fishwick, S., 2012. Seismic structure of the southeast Australian lithosphere from surface and body wave tomography, *Tectonophysics,* **572**, 111–122.

Rawlinson, N. & Kennett, B.L.N., 2008. Teleseismic tomography of the upper mantle beneath the southern Lachlan Orogen, Australia, *Phys. Earth planet. Inter.,* **167**(1-2), 84–97.

Reed, C.A., Gao, S.S., Liu, K.H. & Yu, Y., 2016. The mantle transition zone beneath the Afar Depression and adjacent regions: implications for mantle plumes and hydration, *Geophys. J. Int.,* **205**(3), 1756–1766.

Ringwood, A.E., 1975. *Composition and Petrology of the Earth's Mantle,* 1st edn, pp. 672, MacGraw-Hill.

Simmons, N.A., Myers, S.C., Johannesson, G. & Matzel, E., 2012. LLNL-G3Dv3: global P wave tomography model for improved regional and teleseismic travel time prediction, *J. geophys. Res.,* **117**(B10), doi:10.1029/2012JB009525.

Smith, W. & Wessel, P., 1990. Gridding with continuous curvature splines in tension, *Geophysics,* **55**(3), 293–305.

Sun, M., Fu, X., Liu, K.H. & Gao, S.S., 2018. Absence of thermal influence from the African Superswell and cratonic keels on the mantle transition

zone beneath southern Africa: evidence from receiver function imaging, *Earth planet. Sci. Lett.,* **503,** 108–117.

Taylor, G., Thompson, D.A., Cornwell, D. & Rost, S., 2018. Interaction of the Cyprus/Tethys slab with the mantle transition zone beneath Anatolia, *Geophys. J. Int.,* **216**(3), 1665–1674.

Tschauner, O., Ma, C., Beckett, J.R., Prescher, C., Prakapenka, V.B. & Rossman, G.R., 2014. Discovery of bridgmanite, the most abundant mineral in Earth a shocked meteorite, *Science,* **346**(6213), 1100–1102.

van Stiphout, A.M., Cottaar, S. & Duess, A., 2019. Receiver function mapping of mantle transition zone discontinuities beneath Alaska using scaled 3-D velocity corrections, *Geophys. J. Int.,* **219,** 1432–1446.

Wang, F., Barklage, M., Lou, X., van der Lee, S., Bina, C.R. & Jacobsen, S.D., 2018. HyMaTZ: a Python program for modeling seismic velocities in hydrous regions of the mantle transition zone, *Geochem., Geophys., Geosys.,* **19**(8), 2308–2324.

Yoshizawa, K. & Kennett, B.L.N., 2004. Multimode surface wave tomography for the Australian region using a three-stage approach incorporating finite frequency effects, *J. geophys. Res.,* **109,** B02310, doi:10.1029/2002JB002254.

Yoshizawa, K. & Kennett, B.L.N., 2015. The lithosphere-asthenosphere transition and radial anisotropy beneath the Australian continent, *Geophys. Res. Lett.,* **42,** 3839–3846.

Yu, Y., Gao, S.S., Liu, K.H., Yang, T., Xue, M. & Le, K.P., 2017. Mantle transition zone discontinuities beneath the Indochina Peninsula: implications for slab subduction and mantle upwelling, *Geophys. Res. Lett.,* **44**(14), 7159–7167